

# A study on the energy transfer of a square prism under aeroelastic galloping

H.G.K.G. Jayatunga, B.T. Tan, J. S. Leontini

---

## Abstract

Extracting useful energy from flow induced vibrations has become a developing area of research in recent years. In this paper, we analyse power transfer of an elastically mounted body under the influence of aeroelastic galloping. The system and the power transfer is analysed by numerically integrating the quasi-steady state model equations. The power transfer is analysed for both high ( $Re=22300$ ) and low ( $Re=165$ ) Reynolds numbers cases. At high mass ratios ( $m^* < 50$ ), the system is not frequency dependent. The damping coefficient was shown to be the only control parameter that governed power output. The system is a balance between the power delivered to the system due to hydrodynamic forcing and power removed through mechanical damping which are governed by the hydrodynamic forcing characteristics (i.e. the  $C_y$  as a function of incident angle) and mechanical damping coefficient respectively. A contradictory behaviour is observed at low  $m^*$  between the low and high  $Re$  cases. The forcing due to vortex shedding at low  $Re$  suppresses the galloping excitation and results in a reduced power output. Power output increases as  $m^*$  is reduced for the case with high  $Re$ . The reduction in inertia allows the body to accelerate faster and spend a larger portion of the period at relatively high transverse velocities.

*Keywords:*

---

## 1. Introduction

The search for alternate energy sources which could be categorised under the “green” label has become important area of research in the modern world. Solar, wind power and wave power are some of the examples of these sources. Recently, a new branch of research has been developing to extract energy from flow induced vibrations (Bernitsas et al. (2008)). It has been hypothesized that this technique may work efficiently in areas where regular turbines cannot.

An elastically mounted slender structure such as cylinders which are susceptible to flow-induced vibrations has the potential for energy extraction. With regards to a slender body two common types of flow induced vibrations are Vortex Induced Vibrations (VIV) and aeroelastic galloping. Significant research has been carried out by Bernitsas and his team on extracting useful energy from VIV. Some of their significant work includes investigating the influence of physical parameters such as mass ratio, Reynolds number, mechanical properties (Raghavan and Bernitsas (2011) , Lee and Bernitsas (2011)) and location (effect

of the bottom boundary) (Raghavan et al. (2009)). However, the possibility of extracting energy using aeroelastic galloping has not been thoroughly investigated. Some theoretical work was carried out by (Barrero-Gil et al. (2010)). Utilizing galloping may be a more viable method to harness energy from flow induced vibrations as it is not bounded by a narrow “lock-in” range of reduced velocities (ratio between the freestream velocity and the product of the natural frequency of the system and the characteristic length). This study further explores the possibility of harnessing energy from flow induced vibrations using aeroelastic galloping.

Energy harvesting systems have high damping ratios because the energy generator (e.g electrical generator) puts a significant amount of damping into the system. Therefore it is crucial to investigate the behaviour of aeroleastic galloping scenarios at high damping ratios in order to optimise the system to obtain a acceptable power output. Hence the focus of this paper is concentrated on investigating the mechanical power output of high-damped galloping systems.

According to Païdoussis et al. (2010), Glauert (1919) has provided a criterion for galloping by considering the auto-rotation of an aerofoil. Den Hartog (1956) has provided a theoretical explanation for galloping for iced electric transmission lines. A weakly non-linear theoretical aeroelastic model to predict the response of galloping was developed by Parkinson and Smith (1964) based on the quasi-steady state (QSS) theory. Experimental lift and drag data on a fixed square prism at different angles of attack were used as an input for the theoretical model. It essentially used a curve fit of the transverse force to predict the galloping response. The study managed to achieve a good agreement with experimental data. The QSS model equation when solved analytically using sinusoidal solution method cannot predict cases with low mass ratios. Joly et al. (2012) have observed that finite element simulations shows a sudden change in amplitudes below a critical values of the mass ratio. The Parkinson’s equation was essentially modified to account for the vortex shedding and managed to produce the effects to the amplitude at low mass ratios. Barrero-Gil et al. (2010) have investigated the possibility of extracting power from vibrations caused by galloping using quasi-steady state theory. In the conclusions of that paper it was pointed out that in order to obtain a high power to area ratio, the mass-damping ( $m^*\zeta$ ) parameter should be kept low. Another interesting conclusion was that energy conversion systems which uses galloping could operate over a large range of flow velocities unlike VIV energy harvesting systems where the factor of energy conversion has a strong dependence on the incoming flow velocity.

## Nomenclature

$a_1, a_3, a_5, a_7$	coefficients of the polynomial to determine $C_y$
$C_y$	instantaneous lift
$F_y$	force due to $C_y$
$\rho$	fluid density
$m$	mass of the body
$m_a$	added mass
$c$	damping constant/damping factor
$k$	spring constant
$U_i$	induced velocity
$\theta$	induced angle of incidence
$U$	freestream velocity
$y, \dot{y}, \ddot{y}$	transverse displacement, velocity and acceleration
$A$	displacement amplitude
$\mathcal{A}$	cross sectional area
$F_0$	force due to shedding
$\omega_s$	vortex shedding frequency
$t$	time
$P_{mean}$	mean power
$f = \frac{1}{2\pi} \sqrt{\frac{k}{m}}$	natural frequency of the system
$\omega_n = 2\pi f$	natural frequency of the system
$D$	characteristic length of the body
$m^* = \frac{m}{\rho \times \text{Volume of the body}}$	mass ratio
$U^* = \frac{U}{f \times D}$	reduced velocity
$\zeta = \frac{c}{2m\omega_n}$	damping ratio
$P_t$	power transferred to the body by the fluid
$P_d$	power dissipated due to mechanical damping
$Re$	Reynolds number
$\theta = \tan^{-1}(\frac{\dot{y}}{U})$	instantaneous angle

## 2. Background theory

### 2.1. Mathematical model (*Quasi-steady*)

One of the widely used mathematical model to predict the system response under galloping is the Quasi-steady state (QSS) model, incorporated by Parkinson and Smith (1964) for a square cross section. The equation of motion of the body under galloping is given by Eq.(1). The forcing term  $F_y$  is given by Eq.(2).

$$(m + m_a)\ddot{y} + c\dot{y} + ky = F_y \quad (1)$$



Figure 1: Induced angle of attack on the square prism due to the resultant of free-stream velocity of the fluid and transverse velocity of the body.

$$F_y = \frac{1}{2} \rho U^2 \mathcal{A} C_y \quad (2)$$

In the QSS model  $C_y$  is determined by an interpolating polynomial based on the lift and drag data for flow over a stationary body at various angles of attack. The order of the interpolation polynomial has varied from study to study. For example a 7<sup>th</sup> order polynomial was used in Parkinson and Smith (1964) and 3<sup>rd</sup> order polynomial was used in Barrero-Gil et al. (2009). Ng et al. (2005) concluded that using a 7<sup>th</sup> order polynomial is sufficient and a polynomial higher than that of 7<sup>th</sup> order polynomial neither provides a significantly better result nor does it exhibit an additional amplitudes of oscillation. Thus a 7<sup>th</sup> order interpolating polynomial was incorporated in this present study.

$$C_y(\theta) = a_1 \left( \frac{\dot{y}}{U} \right) + a_3 \left( \frac{\dot{y}}{U} \right)^3 + a_5 \left( \frac{\dot{y}}{U} \right)^5 + a_7 \left( \frac{\dot{y}}{U} \right)^7 \quad (3)$$

Joly et al. (2012) introduced an addition of a sinusoidal forcing function to the hydrodynamic forcing. This enables to model to provide accurate predictions even at low mass ratios where galloping excitation is suppressed or not present. In this study, the forcing due to VIV is incorporated using a sinusoidal forcing function  $F_0 \sin \omega_s t$  added to the RHS of the equation.  $\omega_s$  and  $F_0$  represents shedding frequency and the maximum force due to shedding respectively. Thus, the final equation is given by Eq.(4).

$$(m+m_a)\ddot{y} + c\dot{y} + ky = \frac{1}{2} \rho U^2 \mathcal{A} \left( a_1 \left( \frac{\dot{y}}{U} \right) + a_3 \left( \frac{\dot{y}}{U} \right)^3 + a_5 \left( \frac{\dot{y}}{U} \right)^5 + a_7 \left( \frac{\dot{y}}{U} \right)^7 \right) + F_0 \sin(\omega_s t) \quad (4)$$

This equation could be solved by time integration methods. In this study ‘Ode 45’ routine in MATLAB was used to obtain the solutions. However in certain cases (low mass ratios) ‘Ode 15s’ routine was used when Ode 45 tend to diverge.

## 2.2. Calculation of average power

The dissipated power due to the mechanical damping represents the ideal potential amount of harvested power output. Therefore the mean power output could be given by

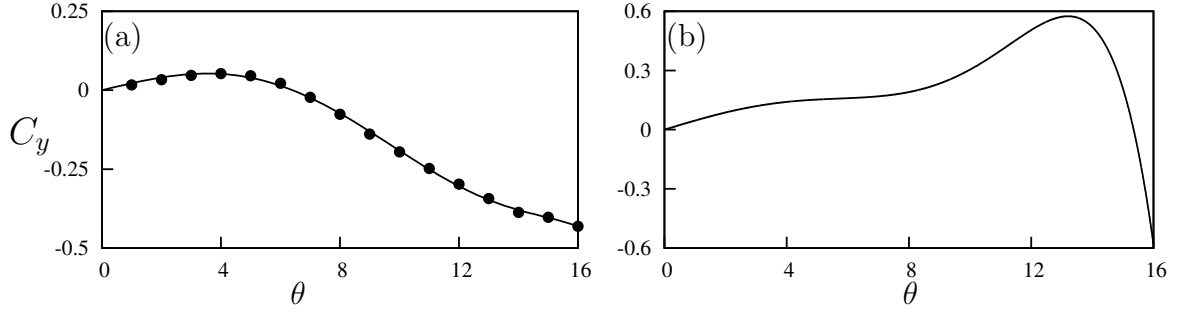


Figure 2: Lift coefficient,  $C_y$ , as a function of incidence angle  $\theta$ , for a static square cross section. (a) Data from simulations at  $Re = 165$  (b) data from Parkinson and Smith (1964) at  $Re = 22300$ . Points ( $\bullet$ ) are measurements from the simulations. The solid lines in both plots are 7th-order interpolating polynomial used to predict the fluid forcing for the QSS model.

Eq.(5).

$$P_{mean} = \frac{1}{T} \int_0^T (c_j y) \dot{y} dt \quad (5)$$

Case	$a_1$	$a_3$	$a_5$	$a_7$
Re=165	1.3	125.3	1825.73	8765.3
Re=22300	2.69	168	1670	59900

Table 1: Coefficient values used in the 7th order interpolation polynomial for high ( $Re = 22300$ ) and low ( $Re = 165$ ) Reynolds numbers. These data are used as input data to calculate the RHS of Eq.4 throughout this study.

### 2.3. Parameters used

The stationary data and the fluid-structure interaction (FSI) data were obtained using a higher order spectral element code to simulate the two-dimensional laminar flow. The Reynolds number was kept at 165 as it was pointed out by Sheard et al. (2009) and Tong et al. (2008) that the 3 dimensional transition for a square cylinder occurs at approximately  $Re=160$ .  $F_0$  was kept at 0.4937 which was obtained by scaling the value used by Joly et al. (2012) with the amplitude ratios of the lift forces obtained at the different Reynolds numbers.

Shedding frequency  $\omega_s$ , was set to 0.98 which was obtained by performing a power spectral analysis of the stationary data at  $0^\circ$ . Stationary  $C_y$  data were obtained at different angles of attack ranging from  $0^\circ$  to  $16^\circ$ . The average power was obtained by using Eq.(5)

and the averaging was done over no less than 20 galloping periods. Predictions of power output at  $Re=22300$  were obtained using coefficients for curve fitting  $C_y$  (Table (1)) from Parkinson and Smith (1964) in order to provide a comparison between high and low Reynolds numbers.  $m^*$  was kept at 1163 for  $Re=22300$  (Similar as Parkinson and Smith (1964)) and  $m^* = 20$  for  $Re=165$ . These parameters were used throughout this study unless otherwise specified.

FSI data were obtained for the oscillating (free-vibration) scenario. The Naiver-Stokes equations were solved using an accelerated frame of reference using the previously mentioned code. A three-step time splitting scheme together with high-order Lagrangian polynomials were used to obtain the solution. The details of the method could be found in Thompson et al. (2006, 1996). This code was incorporated in Leontini et al. (2011, 2007) where it was employed in a fluid-structure interaction problems.

The computational domain consists of 690 quadrilateral macro elements where majority of the elements were concentrated near the square section. A freestream condition was given to the inlet, top and bottom boundaries and the normal velocity gradient was set to zero at the outlet. A convergence study was performed by changing the order of the polynomial ( $p$ -refinement) at  $U^* = 40$  and  $Re=165$ . A 9<sup>th</sup> order polynomial together with a time step of  $\frac{\Delta t U}{D} = 0.001$  was sufficient to ensure an accuracy of 2% with regards to amplitude of oscillation.

### 3. Results

#### 3.1. Stationary data

The stationary  $C_y$  data obtained using flow simulations (Fig.3(a)) have a good agreement with data presented in Joly et al. (2012). In comparison with the 7th order polynomial curve at  $Re=22300$  (Fig.3(b)), several differences could be observed. The peak value of  $C_y$  is significantly low at  $Re=165$  ( $C_y = 0.05$  at  $4^\circ$ ) in comparison with  $Re=22300$  ( $C_y = 0.57$  at  $13^\circ$ ). The inflection point present at  $Re=22300$  could not be observed at  $Re=165$ . This agrees with the findings of Luo et al. (2003). It was concluded by Luo et al. (2003) that hysteresis occur due to the inflection point found in the  $C_y$  curve. Therefore hysteresis is not expected at  $Re=165$ . The range of the incident flow angles where  $C_y$  remain positive is narrow at  $Re=165$  ( $0^\circ < \theta \leq 6^\circ$ ) compared to  $Re=22300$  ( $0^\circ < \theta \leq 15^\circ$ ). This feature is what sustains galloping and power is transferred from the fluid to the supporting structure within this range of incident angles because fluid forces are acting in the direction of travel of the oscillating cylinder. Incident angles beyond this range actually suppresses the galloping and power goes in the opposite direction. Therefore due to the overall smaller  $C_y$  and narrow range of angles where  $C_y$  is positive for  $Re=165$  compared to  $Re=22300$  leads one to expect a significant reduction in power at  $Re=165$  compared to  $Re=2230$ .

#### 3.2. Displacement, velocity and power output as a function of reduced velocity

The quasi-steady analysis data reveals that the displacement amplitude tend to grow with increasing  $U^*$  (Fig.3 (a) and (b)). The onset of galloping is delayed with increasing  $\zeta$  for both high and low Reynolds numbers. This echo the findings of previous studies by

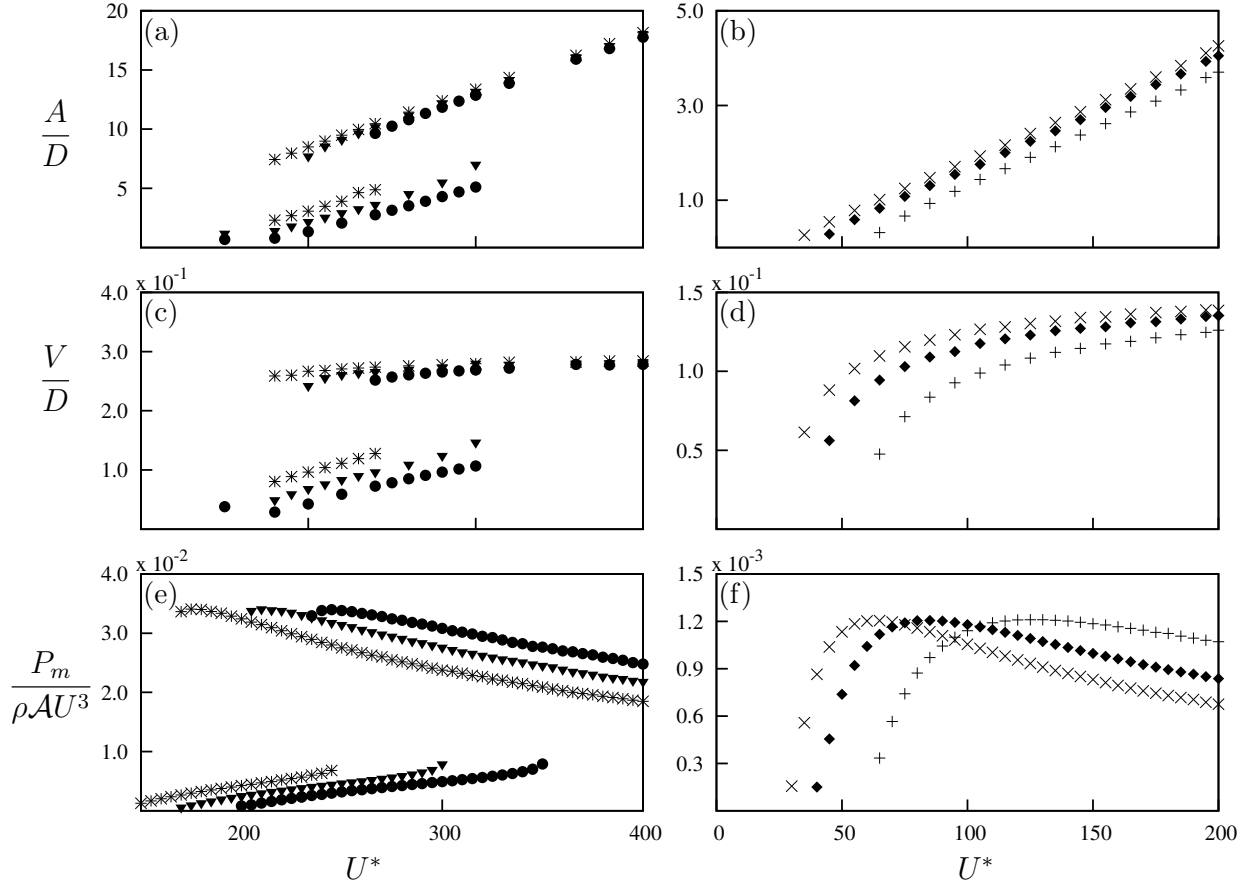


Figure 3: Velocity amplitude, displacement amplitude and mean power as functions of  $U^*$ . Data presented in (a), (c) and (e) were calculated using input data at  $Re = 22300$  obtained by Parkinson and Smith (1964) at three different damping ratios:  $\zeta = 0.0125$  (\*),  $\zeta = 0.015$  ( $\blacktriangledown$ ) and  $\zeta = 0.0175$  ( $\bullet$ ). Data presented in (b),(d) and (f) were obtained using input data at  $Re = 165$  at three different damping ratios:  $\zeta = 0.075$  ( $\times$ ),  $\zeta = 0.1$  ( $\blacklozenge$ ) and  $\zeta = 0.15$  (+). The multiple branches for the higher  $Re$  are due to the hysteresis between two solutions.

Parkinson and Smith (1964) and Barrero-Gil et al. (2010). Hysteresis could be observed for the case with a higher Reynolds number. This was achieved by manipulating the initial conditions (initial displacement) of the system. The upper branch was obtained by giving an initial displacement which was higher than the expected amplitude while the lower branch was obtained by providing a lower initial displacement than the expected amplitude. Although a third state could be achieved theoretically, it was not possible to achieve numerically. This was also observed by Vio et al. (2007).

### *Power vs $U^*$*

The mean power grows, peaks and then reduces as  $U^*$  is increased (Fig.3 (e) and (f)) for each value of  $\zeta$ . The value of  $U^*$  at which the peak power occur increases with  $\zeta$ . However, the magnitude of the peaks remain constant for all the values of  $\zeta$ . Barrero-Gil et al. (2010) also showed a similar trend. The higher Reynolds number case clearly showed hysteresis in the power data. The range of hysteresis tend to increase with increasing  $\zeta$ . It could be observed that unlike VIV the system has no preferred frequency. Although the onset of galloping and the point where peak power occur at different  $U^*$  when the damping ratio is changed, the peak power remains constant regardless of  $U^*$ .

### *3.3. Galloping response and natural frequency*

Now the oscillator equation Eq.(4) is considered from a power perspective. The shedding forces can be neglected because the net effect is negligible as system oscillates at natural frequency which is far from shedding frequency, for the cases that exhibit galloping. It is obvious that the forcing term on LHS of the equation is only dependent on transverse velocity( $\dot{y}$ ) which is essentially the input power of the system. On the RHS, the mechanical damping or system damping is the only term that takes out power at any instant. This could be expressed as the product of the damping force and the velocity ( $P_d$ ). The inertia and the stiffness terms governs the frequency of the system but the forces associated by those terms are conservative forces (i.e there is zero net energy in or out of the system when averaged over a period). Therefore the system is governed by the transverse velocity rather than the natural frequency.

Using  $U^*$  and  $\zeta$  assumes that the system has a preferred frequency because the scale with the natural frequency of the system. The effect of fixing  $\zeta$  and increasing  $U^*$  actually decreases the damping constant for a fixed free-stream velocity. ( $U^* = \frac{U}{f \times D}$ ,  $\zeta = \frac{c}{2m\omega_n}$ ). Both these effects leads to the multiple lines that are horizontally transpose when  $\zeta$  is increased (Fig.3 (e) and (f)). Therefore the effect of  $\zeta$  essentially scales up the damping coefficient for a fixed  $U^*$ .

The data presented in Fig.3 for various damping ratios,  $\zeta$ , can be collapsed into a single line for a particular force characteristic curve (i.e  $C_y$  vs  $\theta$  curve). These collapsed curves were obtained for the velocity amplitude and power by plotting as functions of as a function of the non dimensionalised damping constant  $\frac{c}{\rho A U}$  (Fig 4 (a),(b),(c) and (d)). This further emphasizes that the galloping system is not frequency dependent. It is possible to obtain a different similar power output at different values of  $U^*$  when the damping constant,  $\frac{c}{\rho A U}$ , is kept fixed. An example of this case, as shown in Fig.5, clearly show that



this is a result of similar velocity amplitudes between cases if one were to disregard the high frequencies due to shedding. As mentioned earlier, it is the transverse velocity that determines the energy provided by the fluid forcing and the mechanical damping.

Power could be expressed as the product of force and velocity. Therefore the transferred power from fluid-to-body could be expressed as  $P_t = F_y \dot{y}$ . Similarly the dissipated power due to the mechanical damping could be expressed as  $P_d = (c\dot{y})\dot{y}$ . The time average of these two quantities should be equal due to energy conservation, provided that the mechanical friction is neglected. Analysing the time histories of  $P_t$  and  $P_d$  at key regions (Fig.6) on the mean power vs  $U^*$  provides a detailed explanation for the variation of the output power when the reduced velocity is increased. The key regions consists of region 1 where the  $P_{mean}$  increases with  $U^*$ , region 2 where  $P_{mean}$  becomes maximum and region 3 where  $P_{mean}$  decreases with  $U^*$ . It has been established earlier that the damping factor is a function of  $U^*$ . Therefore it could be derived that  $U^*$  is inversely proportional to damping coefficient. Hence the damping coefficient reduces when you move from region 1 to 3. Fig 2 (a) shows that  $C_y$  and therefore instantaneous force rises until  $4^\circ$  where it peaks and then falls and at around  $6^\circ$  becomes negative. Maximum amount of power could be transferred within the peak region. At the region where the instantaneous force becomes negative it will be opposing the velocity  $\dot{y}$ . Data at  $\zeta = 0.1$ ,  $m^* = 40$  and  $Re=165$  (Fig.7) are analysed as an example.

At region 1 where  $U^* = 90$  the damping constant is high and a clear sinusoidal signal could be observed for both  $P_d$  and  $P_t$  in Fig.7 (a). Fig.7 (d) and (g) shows that  $\theta$  is in line or in phase with  $F_y$ . The velocity amplitude in this case is small and the equivalent incident angle within the range where the hydrodynamic force increases with the incident angle (i.e.  $0 < \theta \leq 4^\circ$  in Fig.2 (a)) Hence both  $P_d$  and  $P_t$  becomes sinusoidal. In this case, power output is limited by the low fluid forces present at low incident angles. In other words damping is significantly high and extracts a lot of power that the velocity amplitude could not grow where the forcing is significant to produce high level of power.

At region 3 ( $U^* = 400$ ) ' $c$ ' is low in comparison with region 1 and 2 which leads to a low mean power output. Fig.7 (c) shows that  $P_t$  becomes negative over some portion of the cycle. This is because  $\theta$  passes the point where both  $\theta$  and  $C_y$  (therefore  $F_y$ ) are positive. The high velocity amplitude leads to the equivalent incident angle  $\theta$ , in this case to exceed the range where  $C_y$  is positive (i.e.  $0 < \theta < 6^\circ$  in Fig.3 (a)). In this portion of the cycle the hydrodynamic force actually opposes the direction of travel and power is transferred from the structure to the fluid during those times. From an energy perspective, the mechanical damping is not sufficient to remove the energy transferred from the fluid to the structure during other times of the cycle because  $\frac{c}{\rho AU}$  is substantially low. Therefore this excess energy is transferred back to the fluid as depicted by the negative region of  $P_d$  in Fig.7 (c)

At region 2 ( $U^* = 165$ ).  $P_t$  is not a pure sinusoidal signal. However, the signal remains periodic. From the time history graph of  $P_t$ , two 'peaks' are present in a single half cycle (Fig 7 (b)). In this case, the velocity amplitude actually exceeds the equivalent incident angle where the hydrodynamic forces peaks (i.e.  $\theta = 4^\circ$  in 3 (a)). The dips in  $P_d$  between the two peaks approximately correspond to the time where the transverse velocity is higher

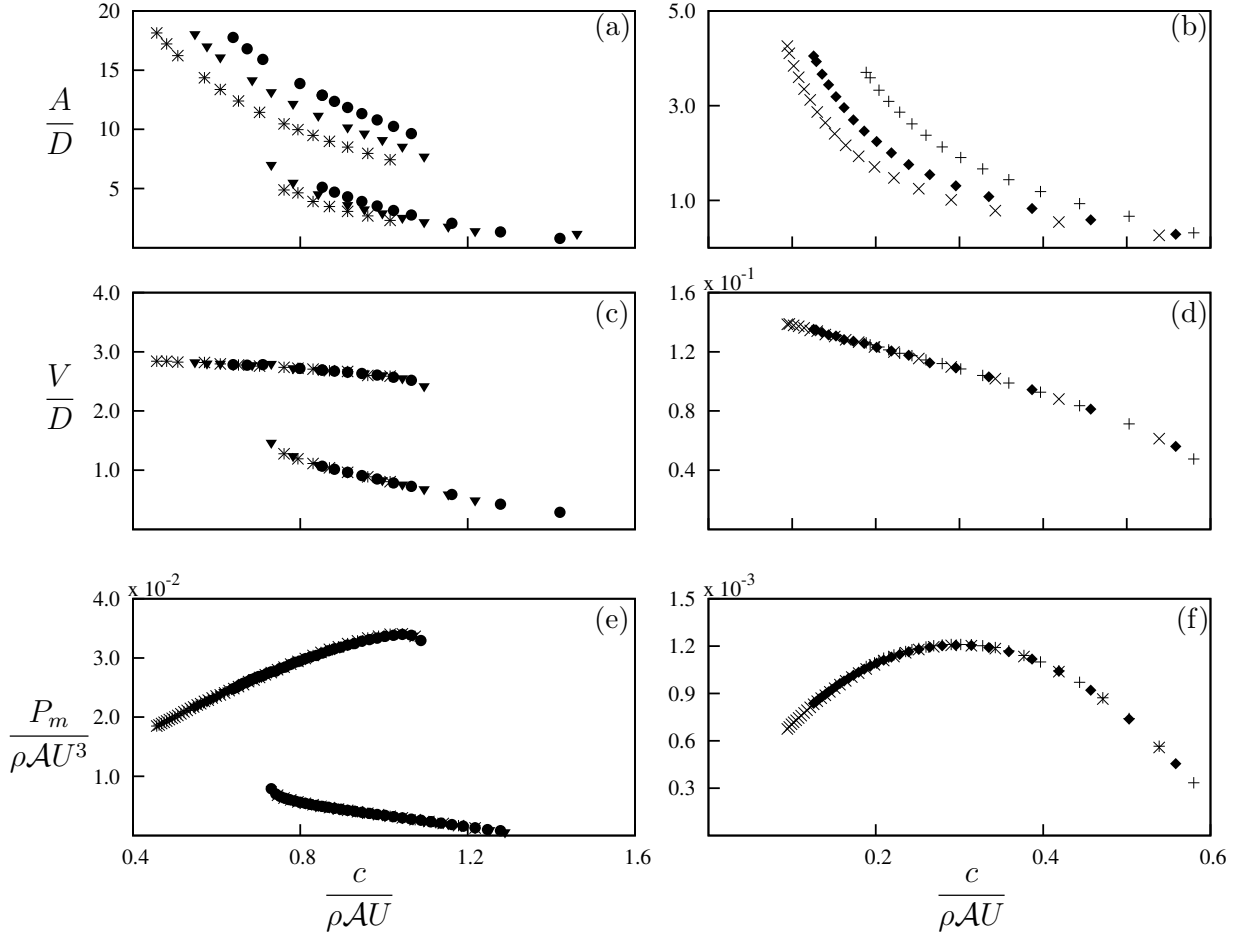


Figure 4: Displacement amplitude, velocity amplitude and mean power as functions of the damping factor. Data presented in (a),(c) and (e) were calculated using input data at  $Re = 22300$  obtained by Parkinson and Smith (1964) at three different damping ratios:  $\zeta = 0.0125$  (\*),  $\zeta = 0.015$  (▼) and  $\zeta = 0.0175$  (●). Data presented in (b), (d) and (f) were obtained using input data at  $Re = 165$  at three different damping ratios:  $\zeta = 0.075$  (×),  $\zeta = 0.1$  (◆) and  $\zeta = 0.15$  (+). The collapsed data implies that there is no frequency selection and the tuning parameter of the mechanical side of the system is the damping constant to obtain an optimum power output.

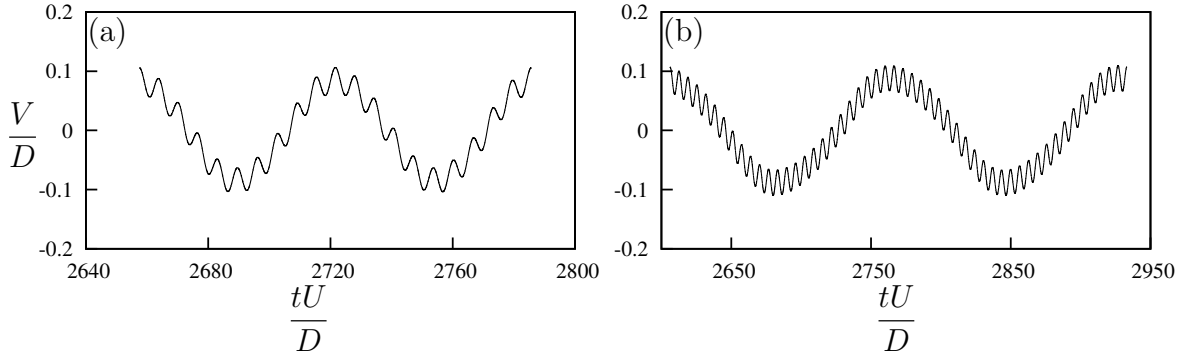


Figure 5: Time histories of velocity at two different  $\zeta$  and  $U^*$  which produce the same mean power ( $1.2 \times 10^{-3}$ ). Data presented in (a) are at  $U^* = 60$ ,  $\zeta = 0.075$  and (b) are at  $U^* = 165$ ,  $\zeta = 0.175$ . Both data sets were obtained using Quasi-steady state assumption using input  $C_y$  parameters at  $Re = 165$ . Shedding is evident in both signals as a high frequency fluctuation but the amplitude of the slower fluctuations remains constant in both cases.

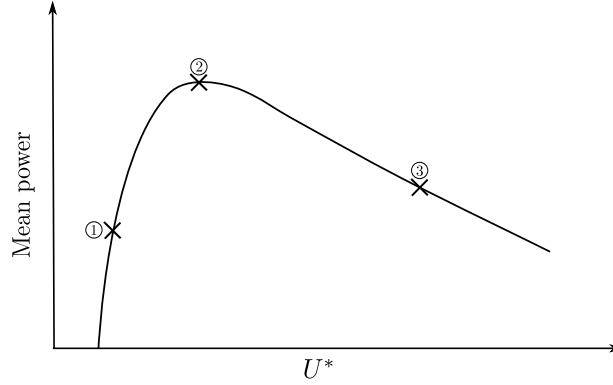


Figure 6: Three key regions taken into account to analyse the time histories of power in a typical mean power vs.  $U^*$  curve at  $Re = 165$ . In region 1, high damping suppresses oscillation, hence the power output is low. In region 2, the damping is close to the optimum for power transfer. In region 3, the low damping means little energy is extracted from the fluid.

than 0.07 and  $F_y$  is decreasing with increasing transverse velocity. The mean power output is at its maximum. This is due to the fact that this region is a best compromise between region 1 and 3. The damping is substantially high to obtain a high power output while not too high to hinder the induced angle of attack entering the region where the forcing is high.

### 3.4. Effect of $m^*$

The maximum mean power at different  $m^*$  (Fig.8(a)) was constant for  $m^* < 30$  in the low  $Re$  case. However, at  $m^* \leq 30$ , the power output reduces with reducing  $m^*$  across the parameter range. However, when the sinusoidal forcing function in Eq.1 which cater for the vortex shedding was disregarded, the reduction in power could not be observed Fig.8(b).

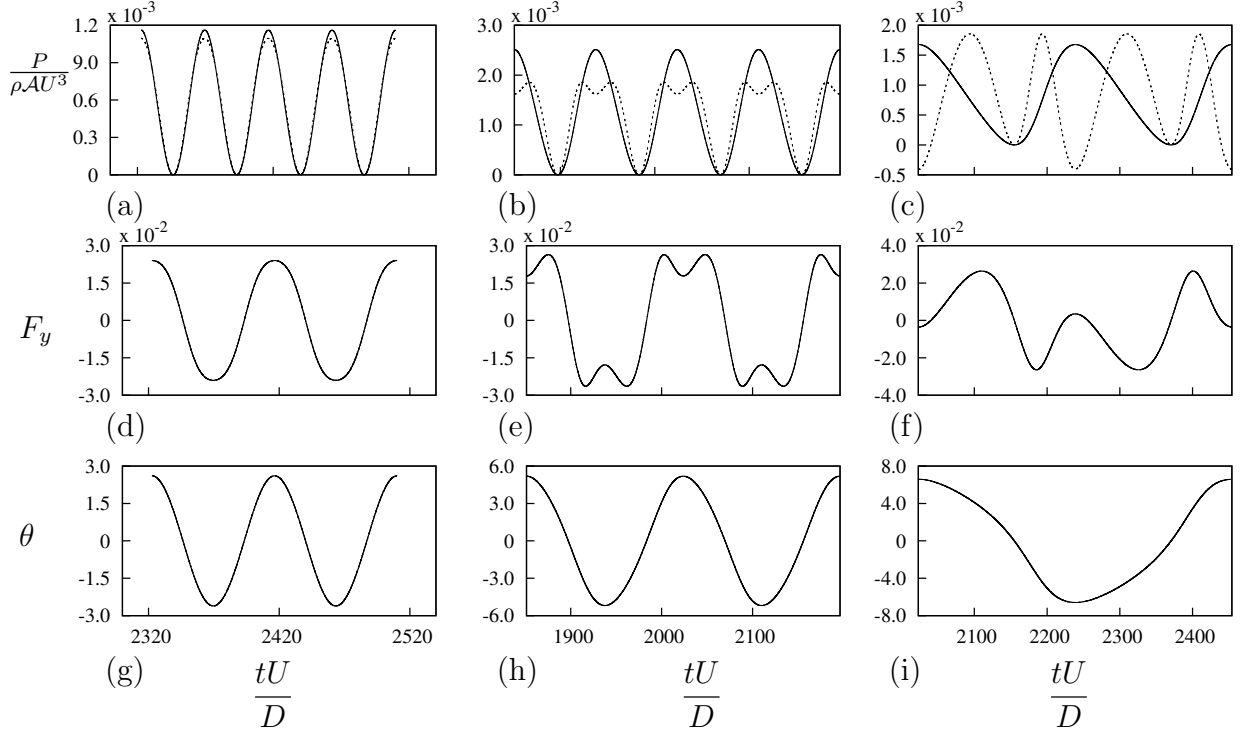


Figure 7: Time histories of  $P_t$ ,  $P_d$ ,  $F_y$  and  $\theta$  at  $U^* = 90, 165$  and  $400$ . Data was obtained at  $\zeta = 0.1$ ,  $m^* = 40$  and  $Re=165$ . The time histories of  $P_t$  (—) and  $P_d$  (---) are presented for: (a)  $U^* = 90$ ; (b)  $U^* = 165$ ; (c)  $U^* = 400$ . Time histories of the instantaneous force  $F_y$  for: (d)  $U^* = 90$ ; (e)  $U^* = 165$ ; (f)  $U^* = 400$ . Time histories of the instantaneous angle  $\theta$  for: (g)  $U^* = 90$ ; (h)  $U^* = 165$ ; (i)  $U^* = 400$ .

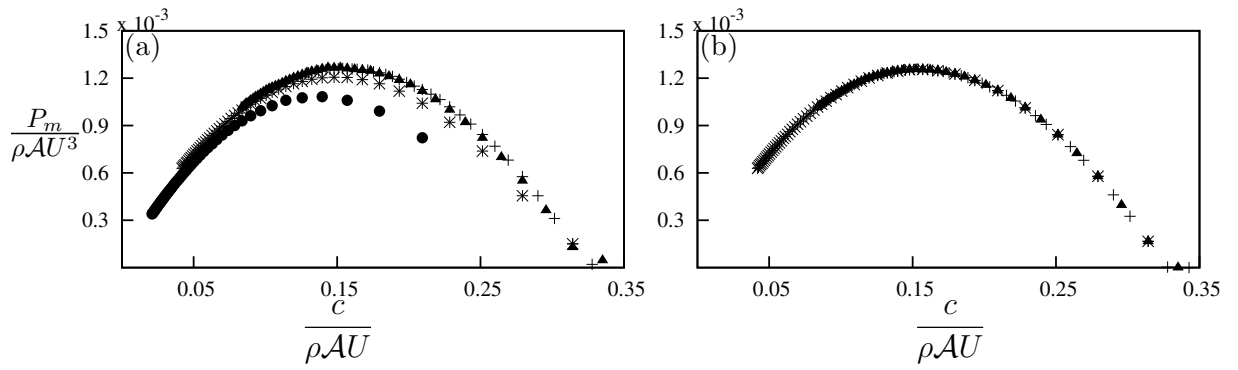


Figure 8: Mean power as a function of damping factor. Data are presented at  $m^* = 10$  (●),  $m^* = 20$  (\*),  $m^* = 40$  (▲),  $m^* = 60$  (+) at  $Re = 165$  (a) with and (b) without the shedding term in Eq.4. A reduction of maximum mean power can be observed when  $m^* < 40$  with shedding while the maximum power is essentially independent of  $m^*$  when shedding is disregarded.

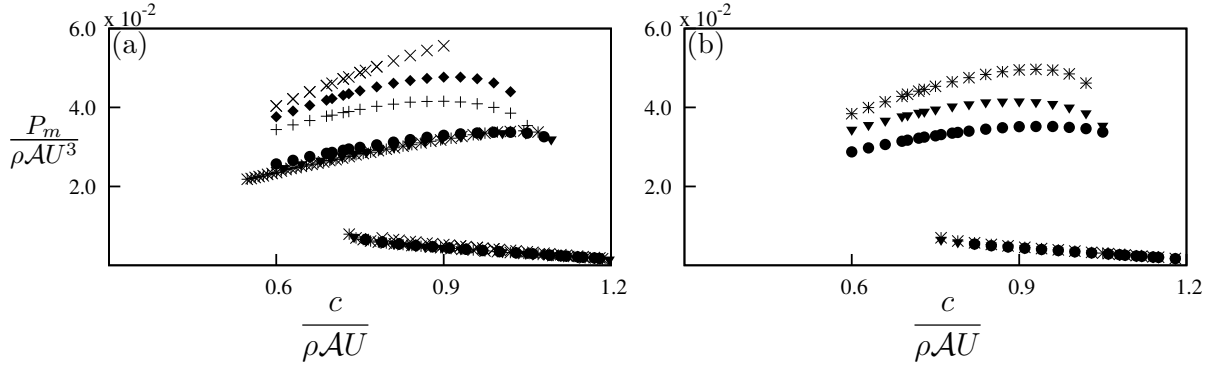


Figure 9: Mean power as a function of damping factor. Data presented in both (a) and (b) were calculated using input data at  $Re=22300$  Parkinson and Smith (1964) where (a) shows mean power data at six different mass ratios:  $m^* = 1164$  (\*),  $m^* = 100$  (▼),  $m^* = 50$  (●),  $m^* = 10$  (+),  $m^* = 5$  (■) and  $m^* = 1$  (×) at  $U^*=175$ . Data presented in (b) shows mean power data at three different reduced velocities:  $U^*=75$  (●),  $U^*=175$  (▼) and  $U^*=375$  (\*) at  $m^* = 10$ . The maximum mean power tend to increase with decreasing  $m^*$  as well as increasing  $U^*$  at low  $m^*$ .

The suppression of galloping response at low  $m^*$  due to the presence of vortex shedding has previously been observed by Joly et al. (2012). This is a non-linear interaction between the forcing that drives the galloping excitation and the forcing as a result of vortex shedding. The forcing associated with vortex shedding is significantly larger and at a higher frequency than the forcing that drives galloping. Systems with low  $m^*$  do not have enough inertia to fully sustain the galloping excitation over the longer period.

At  $Re=22300$  power output started to increase for cases with  $m^* < 50$ . The overall mean power tend to increase as the  $m^*$  was decreased when  $U^*$  was kept constant (Fig9 (a)). The same effect was observed when  $U^*$  was increased keeping  $m^*$  constant (9 (b)). It should be noted that the influence of  $U^*$  was observed only for low mass ratios. The velocity time traces of example cases of both scenarios presented in Fig.10 and 11 shows that essentially the same phenomenon occurring in both cases whereby the velocity signal tend to shift from a sinusoidal signal towards a square wave. The corresponding displacement signal tend to become more like a triangular wave. When the inertia of the system reduces, the body can accelerate faster thus attaining higher velocities more rapidly and spend a higher proportion of the period at a high velocity. Higher velocities are favourable because they result in higher instantaneous hydrodynamic forcing and power output from mechanical damping. However, the velocity is limited by the characteristic of the hydrodynamics forcing which reaches a maximum and then decreases past an incident angle of  $6^\circ$  degrees which correspond to a transverse velocity of  $\frac{\dot{y}}{U} =$ . Increasing  $U^*$  effectively reduces the stiffness of the system and lengthen the period, thus again allowing a larger portion of the period to be at a high velocity which favours power output. For the case of fixing  $U^*$  and decreasing  $m^*$  in (Fig9 (a)), the lengthening of the period is associated with the added mass which is kept constant at ??? being more dominant on the overall mass of the system when  $m^*$  is reduced.

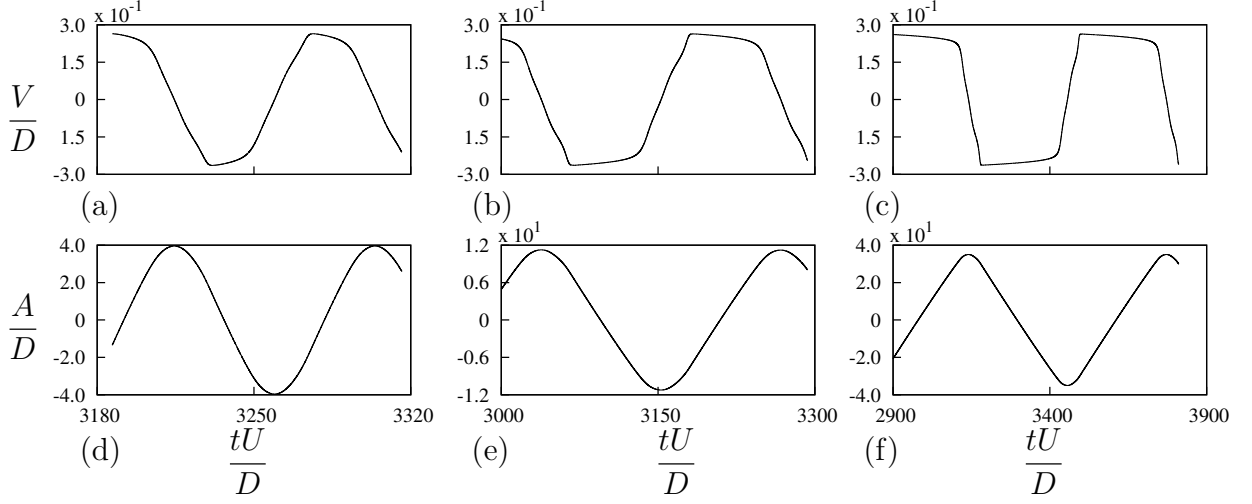


Figure 10: Time histories of displacement and velocity at  $Re=22300$ ,  $U^*=175$  and  $\frac{c}{\rho A U} = 9.3 \times 10^{-1}$ . The velocity time histories are presented for: (a)  $m^* = 1164$ ; (b)  $m^* = 10$ ; (c)  $m^* = 5$ . The time histories of displacement are presented for: (d)  $m^* = 1164$ ; (e)  $m^* = 10$ ; (f)  $m^* = 5$ . As the mass ratio decreases the velocity signal tend to transform from a sinusoidal towards a square signal and the displacement signal tend to move towards a triangular signal due to reduction in inertia.

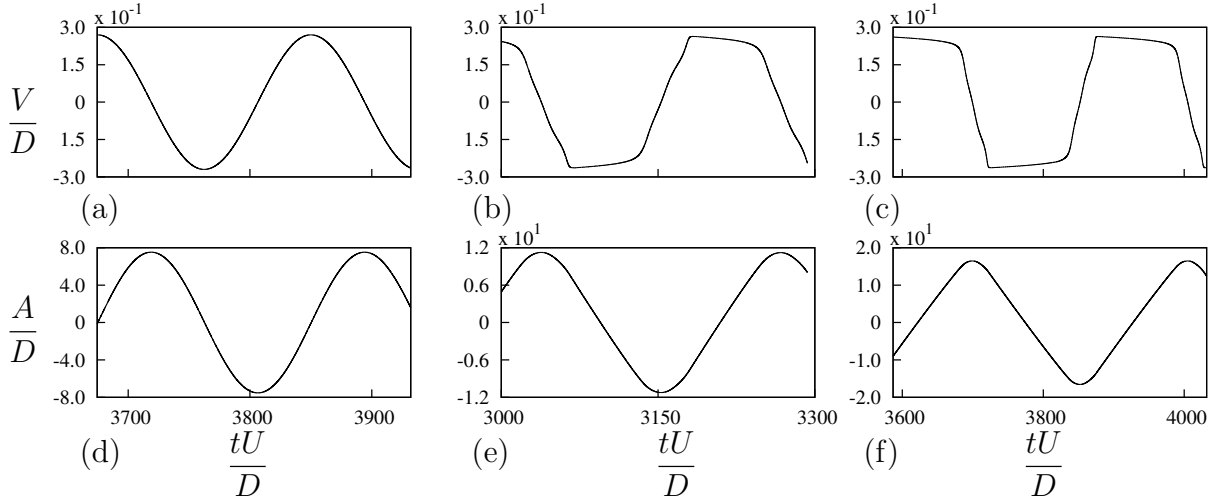


Figure 11: Time histories of displacement and velocity at  $Re=22300$ ,  $m^* = 10$  and  $\frac{c}{\rho A U} = 9.3 \times 10^{-1}$ . The velocity time histories are presented for: (a)  $U^*=75$ ; (b)  $U^*=175$  (c)  $U^*=375$ . The time histories of displacement are presented for: (d)  $U^*=75$ ; (e)  $U^*=175$ ; (f)  $U^*=375$ . As the mass ratio decreases the velocity signal tend to transform from a sinusoidal towards a square signal and the displacement signal tend to move towards a triangular signal.

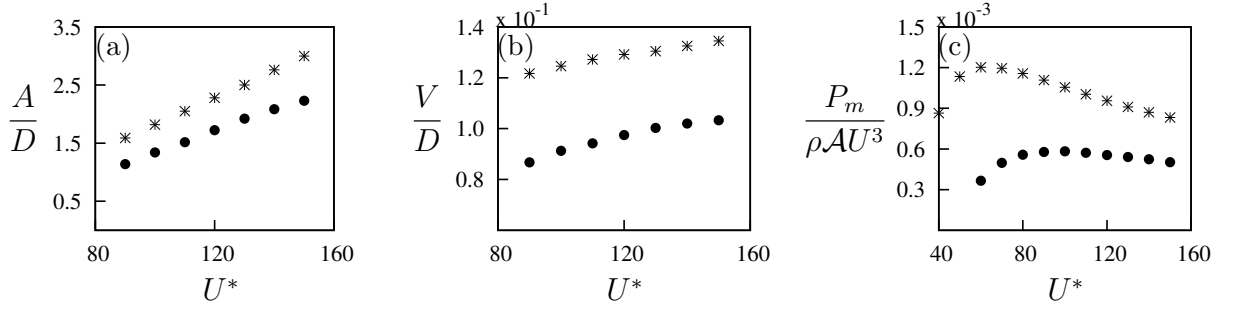


Figure 12: Comparison of data generated using the quasi-static theory (\*) and full DNS simulations (●). (a) Displacement amplitude, (b) velocity amplitude and (c) mean power as functions of  $U^*$ . Data were obtained at  $Re = 165$  and  $\zeta = 0.075$ . An average difference of 34% is observed for both displacement and velocity amplitude. However, the essential physics i.e the rise and fall of mean power, is captured by DNS simulations.

### 3.5. Comparison with FSI simulations

Similar trends were captured for both displacement and velocity amplitudes between QSS and FSI simulations (Fig. 12(a) and 12(b)). Quantitatively a large discrepancy (average of 30%) could be observed between QSS and FSI data. Therefore the power also becomes significantly low in FSI data (Fig.12 (c)). However, the FSI data (Fig.12 (c)) were able to produce the main the rise and the fall of mean power when  $U^*$  was increased. The reasoning behind this fact is that galloping is weak at  $Re = 165$  and therefore fluid damping has a significant effect. It was reported by Barrero-Gil et al. (2009) that galloping only starts to occur at  $Re \geq 159$ . As power is function of  $(\dot{y})^2$  the error between QSS and FSI power becomes significantly large.

## 4. Conclusion

In this paper, the power transfer of a square body under aero elastic galloping is analysed by solving the quasi-steady state model equations through numerical integration. The power output of the system is not dependent on  $U^*$  or natural frequency of the system, but dependent on the transverse velocity amplitude of the system. This is shown by the collapsed plots in terms of non-dimensionalised damping constant (using flow parameters). By analysing key regions of the power vs  $U^*$  curve it could be concluded that in order to obtain an optimum power output, the damping constant  $(\frac{c}{\rho A U})$  should be high, but not excessive until it hinders the galloping from reaching induced angles of attack where the forcing is significant. The effect of mass ratio could also be observed where at  $Re = 165$ . The mean power tends to decrease at  $m^* < 50$  which was found out to be an influence of vortex shedding. At  $Re = 22300$  an opposite result could be observed where the mean power tends to increase with decreasing mass ratio as well as the mean power tends to increase with increasing  $U^*$  at low mass ratios. The cause for this was found out to be the fact that when the mass ratio decreases, due to the lower inertia the velocity time trace tends to move from a sinusoidal signal towards a square signal where it sustains high velocities for longer periods of time which leads to a higher mean power output.

- Barrero-Gil, A., Alonso, G., Sanz-Andres, A., Jul. 2010. Energy harvesting from transverse galloping. *Journal of Sound and Vibration* 329 (14), 2873–2883.
- Barrero-Gil, A., Sanz-Andrés, A., Roura, M., Oct. 2009. Transverse galloping at low Reynolds numbers. *Journal of Fluids and Structures* 25 (7), 1236–1242.
- Bernitsas, M. M., Raghavan, K., Ben-Simon, Y., Garcia, E. M. H., 2008. VIVACE (Vortex Induced Vibration Aquatic Clean Energy): A new concept in generation of clean and renewable energy from fluid flow. *Journal of Offshore Mechanics and Arctic Engineering* 130 (4), 041101–15.
- Den Hartog, J. P., 1956. *Mechanical Vibrations*. Dover Books on Engineering. Dover Publications.
- Glauert, H., 1919. The rotation of an aerofoil about a fixed axis. Tech. rep., Advisory Committee on Aeronautics R and M 595. HMSO, London.
- Joly, A., Etienne, S., Pelletier, D., Jan. 2012. Galloping of square cylinders in cross-flow at low Reynolds numbers. *Journal of Fluids and Structures* 28, 232–243.
- Lee, J., Bernitsas, M., Nov. 2011. High-damping, high-Reynolds VIV tests for energy harnessing using the VIVACE converter. *Ocean Engineering* 38 (16), 1697–1712.
- Leontini, J. S., Lo Jacono, D., Thompson, M. C., Nov. 2011. A numerical study of an inline oscillating cylinder in a free stream. *Journal of Fluid Mechanics* 688, 551–568.
- Leontini, J. S., Th, M. C., Hourigan, K., Apr. 2007. Three-dimensional transition in the wake of a transversely oscillating cylinder. *Journal of Fluid Mechanics* 577, 79.
- Luo, S., Chew, Y., Ng, Y., Aug. 2003. Hysteresis phenomenon in the galloping oscillation of a square cylinder. *Journal of Fluids and Structures* 18 (1), 103–118.
- Ng, Y., Luo, S., Chew, Y., Jan. 2005. On using high-order polynomial curve fits in the quasi-steady theory for square-cylinder galloping. *Journal of Fluids and Structures* 20 (1), 141–146.
- Païdoussis, M., Price, S., de Langre, E., 2010. *Fluid-Structure Interactions : Cross-Flow-Induced Instabilities*. Cambridge University Press.
- Parkinson, G. V., Smith, J. D., 1964. The square prism as an aeroelastic non-linear oscillator. *The Quarterly Journal of Mechanics and Applied Mathematics* 17 (2), 225–239.
- Raghavan, K., Bernitsas, M., Apr. 2011. Experimental investigation of Reynolds number effect on vortex induced vibration of rigid circular cylinder on elastic supports. *Ocean Engineering* 38 (5-6), 719–731.



- Raghavan, K., Bernitsas, M. M., Maroulis, D. E., 2009. Effect of Bottom Boundary on VIV for Energy Harnessing at  $8 \times 10^3 < Re < 1.5 \times 10^5$ . *Journal of Offshore Mechanics and Arctic Engineering* 131 (3), 031102.
- Sheard, G. J., Fitzgerald, M. J., Ryan, K., Jun. 2009. Cylinders with square cross-section: wake instabilities with incidence angle variation. *Journal of Fluid Mechanics* 630, 43.
- Thompson, M., Hourigan, K., Sheridan, J., Feb. 1996. Three-dimensional instabilities in the wake of a circular cylinder. *Experimental Thermal and Fluid Science* 12 (2), 190–196.
- Thompson, M. C., Hourigan, K., Cheung, A., Leweke, T., Nov. 2006. Hydrodynamics of a particle impact on a wall. *Applied Mathematical Modelling* 30 (11), 1356–1369.
- Tong, X., Luo, S., Khoo, B., Oct. 2008. Transition phenomena in the wake of an inclined square cylinder. *Journal of Fluids and Structures* 24 (7), 994–1005.
- Vio, G., Dimitriadis, G., Cooper, J., Oct. 2007. Bifurcation analysis and limit cycle oscillation amplitude prediction methods applied to the aeroelastic galloping problem. *Journal of Fluids and Structures* 23 (7), 983–1011.